PNAS

Cross-sections of doubly curved sheets as confined elastica

Mengfei He[a,b,1] (ID), Vincent Démery[c,d] (ID), and Joseph D. Paulsen[a,b] (ID)

Although thin films are typically manufactured in planar sheets or rolls, they are often forced into three-dimensional (3D) shapes, producing a plethora of structures across multiple length scales. To understand this complex response, previous studies have either focused on the overall gross shape or the small-scale buckling that decorates it. A geometric model, which considers the sheet as inextensible yet free to compress, has been shown to capture the gross shape of the sheet. However, the precise meaning of such predictions, and how the gross shape constrains the fine features, remains unclear. Here, we study a thin-membraned balloon as a prototypical system that involves a doubly curved gross shape with large amplitude undulations. By probing its side profiles and horizontal cross-sections, we discover that the mean behavior of the film is the physical observable that is predicted by the geometric model, even when the buckled structures atop it are large. We then propose a minimal model for the horizontal cross-sections of the balloon, as independent elastic filaments subjected to an effective pinning potential around the mean shape. Despite the simplicity of our model, it reproduces a broad range of phenomena seen in the experiments, from how the morphology changes with pressure to the detailed shape of the wrinkles and folds. Our results establish a route to combine global and local features consistently over an enclosed surface, which could aid the design of inflatable structures, or provide insight into biological patterns.

elastic sheets | inflated surfaces | water balloons | wrinkle-fold transition | gross shape

Complex patterns of wrinkles, crumples, and folds can arise when a thin solid film is stretched (1–3), compacted (4–7), stamped (8–10), or twisted (11–13). These microstructures arise to solve a geometric problem: they take up excess length at a small scale to facilitate changes in length imposed at a larger scale, by boundary conditions at the edges or by an imposed metric in the bulk. When the confining potential is sufficiently soft, like that presented by a liquid, the sheet can have significant freedom to select the overall response that the small-scale features decorate (11, 14–21). Understanding how gross and fine structures are linked, especially in situations with large curvatures and compression, remains a frontier in the mechanics and geometry of thin films.

To date, the dominant approach has been to treat gross and fine structures separately. For example, tension-field theory (22) accounts for the mechanical effect of wrinkling on the stress and strain fields, while ignoring the detailed deformations at the scale of individual buckles. Recent work (3) has established how to calculate the energetically favored wrinkle wavelength anywhere within a buckled region. But owing to geometric nonlinearities, these approaches have been limited to situations with small slopes and a high degree of symmetry, and they assume small-amplitude sinusoidal wrinkles at the outset. A geometric model was recently developed (17, 23) for situations where energy external to the sheet—like a liquid surface tension or gravity—ultimately selects the gross shape. Although this model can address situations with arbitrary slopes, it is typically agnostic to the exact form of the fine structures. Moreover, it is unclear what surface the geometric model precisely predicts in the presence of finite amplitude wrinkles or folds.

At the small scale, significant progress has been made on understanding oscillating buckled features by analyzing an inextensible rod attached to a fluid or solid foundation (2, 24). This approach can predict the energetically favored wavelength of monochromatic wrinkles, but much less is known about the selection of more complex or evolving microstructures. Morphological transitions, like the formation of localized folds, have been largely analyzed on planar substrates (25–28), and it is not known how they are modified when the gross shape is curved and can freely deform (14).

Here, we elucidate the interplay of the gross and fine structures of a strongly deformed thin sheet by studying a water balloon made by thin membranes that strongly resist stretching (Fig. 1). We obtain a wide range of deformations by varying the internal air

Significance

Understanding how a featureless planar solid film selects a complex morphology is an important fundamental challenge. In particular, it remains unclear how the selection of an overall three-dimensional shape constrains the behavior of smaller-scale wrinkles or folds. Here, we investigate a prototypical system consisting of a thin-membraned balloon that is partially filled with water and pressurized with air. We propose a quasi-two-dimensional model that captures an array of features seen in the experiments, from the shapes of individual folds to how the membrane morphology changes with pressure. Our results establish a route to analyzing complex film morphologies across scales.
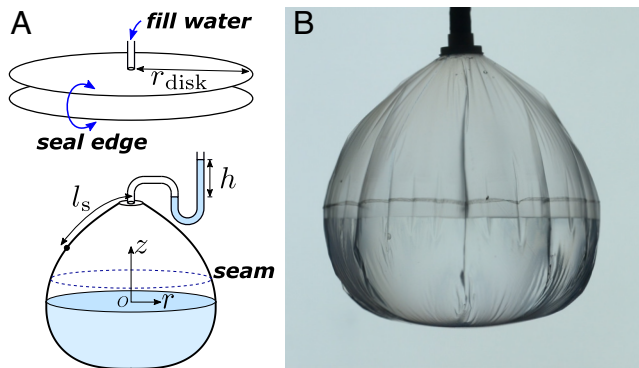
Fig. 1. (A) We make partially filled water balloons by sealing two circular sheets of radius r_{disk} that bend easily but strongly resist stretching. We vary the air pressure inside the balloon, which we measure using the height h of a water column in a U-shaped tube. We use cylindrical coordinates (r, z), and we denote the arclength from the top of the balloon as l_s. (B) Side-view photograph of the setup with water volume $V_{\text{water}} = 277.9$ mL and air pressure $p = 276$ Pa.

pressure and the volume of liquid in the balloon. Despite the complex surface arrangements, a simple geometric model omitting the bending cost captures the mean shape, which we define as the azimuthal average over the small-scale wrinkles and folds. The observed side-view profile of a balloon (Figs. 1B and 2), on the other hand, may differ from the mean shape due to surface fluctuations. We show how the finite wrinkle amplitude can be accounted for and combined with the mean behavior to predict the outer envelope of the wrinkled balloon, in agreement with our experiments. To understand the buckled microstructure in more detail, we model a horizontal cross-section of the balloon as an effective filament pinned to the prediction of the geometric model. Remarkably, our parsimonious model quantitatively captures the fine structures of the balloon, while retaining the agreement between the mean shape and the prediction of the geometric model. We measure the size of the self-contacting loops at the tips of the folds that form at high pressures (Fig. 5A), which further supports our treatment of the horizontal cross-sections as elastic filaments. These results provide a paradigmatic example of how to analyze gross shape and fine structures in a unified approach, for strongly curved sheets.

1. Experimental Setup

We construct closed membranes by sealing together disks of initially planar plastic sheets of radius $r_{\text{disk}} = 83$ mm (Fig. 1). The material outside the seal is then trimmed off, and a nylon washer of radius $r_{\text{top}} = 8$ mm is glued to the center of the top layer for hanging the bag and connecting a tube that can supply air and water into the bag. The same tube is connected to a custom manometer made from two plastic cylinders connected by a U-shaped tube; the difference in water height h allows us to measure the overpressure via the hydrostatic pressure difference $p = \rho g h$ (Fig. 1A). Once inflated, the balloon transforms from a flat initial state to a strongly curved global shape with a complex arrangement of surface structures (Fig. 1B).

2. Geometric Model for Gross Shape

To capture the side-view profiles of the balloons, we use a simple *geometric model* (17, 23, 29) that idealizes the balloon as a smooth, axisymmetric surface $r(z)$ with no surface fluctuations (Fig. 1A). This effective surface is free to bend, inextensible, and free to compress, as compressional stresses are readily relieved by wrinkles and folds. This model is termed "geometric" because it does not involve the elastic moduli of the sheet. Assuming the entire balloon is wrinkled so that the circumferential tension vanishes everywhere, tangential force balance implies that the physical longitudinal stress in the balloon follows $T_s = f/l_s$, where f is a constant with the dimension of force, and l_s the meridian arc-length from the top center to the point in question (Fig. 1A) (22, 30–34). The effective surface carries an effective longitudinal stress T_{eff} which is related to the physical stress through the ratio of the physical to the effective arclengths:

$$T_{\text{eff}} = \frac{l_s}{r} T_s = \frac{f}{r}. \quad [1]$$

Normal force balance relates this longitudinal tension to the curvature of the surface κ in the longitudinal direction and the local pressure drop across the membrane: $\kappa T_{\text{eff}} = \Delta p$. Denoting derivatives with respect to z as primes, the longitudinal curvature is given by $\kappa = -r''/(1 + r'^2)^{3/2}$. Setting $z = 0$ as the water level, the local pressure drop is given by p for $z > 0$ and $p - \rho g z$ for $z < 0$. Using Eq. 1, the normal force balance thus reads
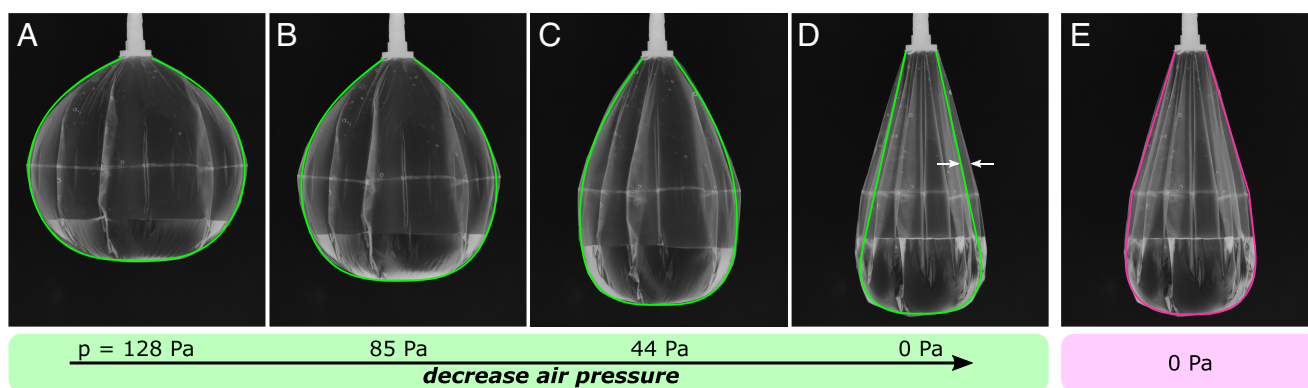
Fig. 2. (A–D) Side-view photographs of a balloon filled with $V_{\text{water}} = 100.4$ mL of water at various internal pressures from $p = 128$ Pa to 0 Pa. Image grayscale inverted for clarity. Green curves: Predictions from the geometric model, Eqs. **??** at the corresponding pressures with no free parameters. The agreement is very good at high pressures, but there is a significant discrepancy at $p = 0$. (E) Pink curve: Adding the amplitude of the wrinkled envelope, Eq. 2 to the geometric model gives good agreement with the side-view profile of panel (D).

Fig. 3. Cross-section model captures the morphological features of the balloon cross-sections. (A) Horizontal cross-section shapes measured by scattering a sheet of laser light at a fixed distance $z_{top} - z = 39.4$ mm below the top of a balloon with $V_{water} = 100.0$ mL, which is gradually deflating from $p = 278$ Pa to 0 Pa. The photographs are tinted an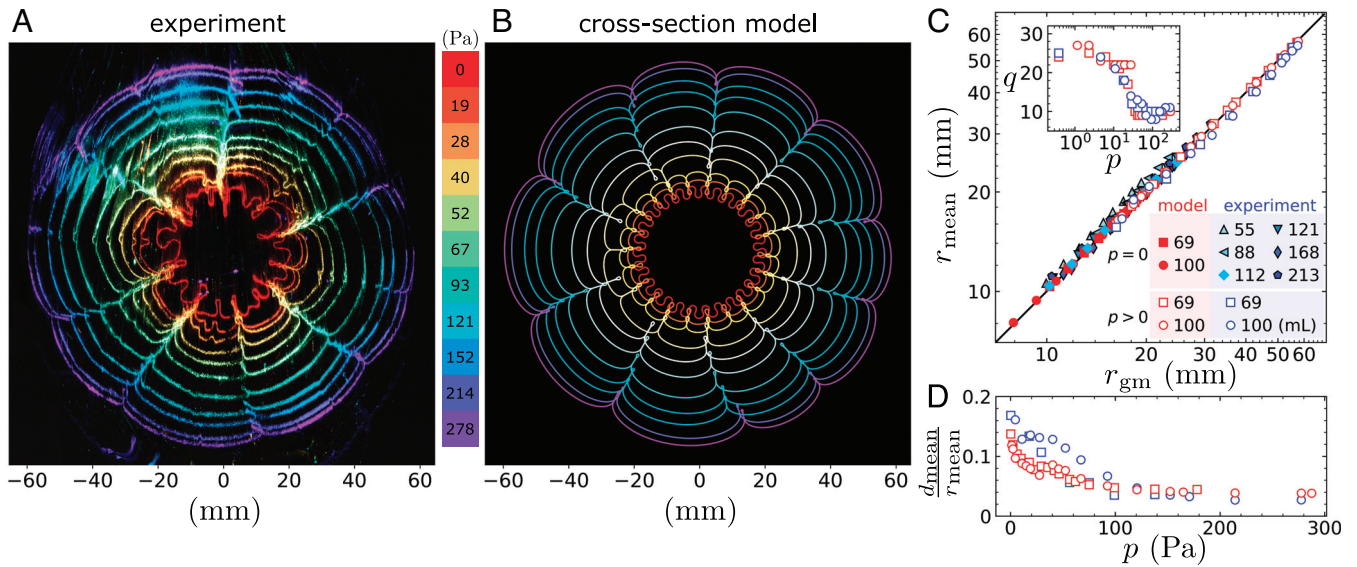d superimposed to compare the different morphologies. (B) Shapes from the cross-section model. All physical parameters (pressure, bending modulus, length of cross-sections, volume of water) were set to match the conditions in panel (A), and a single $\eta = 15$ in Eq. **4** was selected by matching the wavenumber with experiment at high pressures. (C) The average distance of a cross-section to its centroid, r_{mean}, versus the prediction of the geometric model, r_{gm}, in the same z−plane. The data span various cross-sections in different balloons made by produce bags (markers with black edges) or food wrap. Blue markers: experimental measurements. Red markers: cross-section model. Filled markers: $p = 0$. Open markers: $p > 0$. Inset: wavenumber q versus pressure, showing that the cross-section model captures the wrinkle-fold transition. (D) The average fractional protrusion of a cross-section, d_{mean}/r_{mean}, versus pressure. The cross-section model reproduces the trend in the experiments, where the data decay quickly upon inflation. This trend explains how the geometric model can match the side-view profiles at high pressures (Fig. 2 A–C).

$$-\frac{fr''}{r(1+r'^2)^{3/2}} = \begin{cases} p & 0 < z < z_{top} & \textbf{[2a]} \\ p - \rho g z & z_{bot} < z < 0. & \textbf{[2b]} \end{cases}$$

We denote z_{top}, z_{bot} as the top and bottom coordinates of the balloon. Eq. **[2]** are then two second-order ODE's with three parameters f, z_{top} and z_{bot} unknown a priori and hence should be supplemented with seven boundary conditions: $r(0_+) = r(0_-)$ and $r'(0_+) = r'(0_-)$ at the water level, $r(z_{top}) = r_{top}$, $r(z_{bot}) = 0$ and $r'(z_{bot}) \rightarrow \infty$ at the top and the bottom of the balloon, together with the sheet inextensibility constraint $r_{top} + \int_{z_{bot}}^{z_{top}} \sqrt{1 + r'^2} dz = 2r_{disk}$ and a prescribed water volume $\int_{z_{bot}}^{0} \pi r^2 dz = V_{water}$.

Eq. **[2]** are integrated numerically using the explicit Runge–Kutta method of order 5 implemented in the function *solve_ivp* of the package integrate in SciPy (35, 36). The solutions, which we denote as $r_{gm}(z)$, are plotted in Fig. 2 over the corresponding images. This comparison is done with no free parameters. There is an excellent agreement between the numerical predictions and the apparent shape of the balloon at high pressure, despite the complex surface arrangements. However, the agreement is poor at low pressure, as shown by the $p = 0$ case in Fig. 2D. To understand this apparent discrepancy at low air pressures, we turn to the investigation of the fine structure of the balloon.

3. Cross-Sections

We obtain horizontal cross-sections of a balloon at a fixed vertical distance from the top by scattering a sheet of laser light into the system. These cross-sections are then colorized and superimposed to highlight the morphological change as a function of pressure (Fig. 3A). The image shows a transition in the fine structure, starting from folds at large pressure to wrinkles at lower pressure, with an increase of the wavenumber.

For each contour, we identify the center of the balloon with the centroid of the contour, and then measure r_{mean}: the mean distance between the contour and the center of the balloon. Fig. 3C compares the measured r_{mean} versus the prediction of the geometric model r_{gm} in the same plane. The agreement shows that the geometric model accurately predicts the mean shape of the balloon surface. This agreement is robust; the data include cross-sections at multiple vertical locations in the deflated balloon, and different pressures in the inflated balloons, and we have also varied the membrane material and water volume.

To quantify the difference between the mean shape of the balloon and the apparent profile, we measure the average protrusion d_{mean} of each cross-section, which we define to be the average amplitude of the local maxima of each contour. Fig. 3D shows that d_{mean} decays rapidly with increasing pressure. Taken together, the results in Fig. 3 C and D resolve the apparent discrepancy at low pressure between the geometric model and the side-view profiles in Fig. 2. Namely, the side-view profile is given by the mean shape plus the amplitude of the wrinkly undulations, $r_{gm} + d_{mean}$. Fig. 3D shows that these undulations can be rather large at zero pressure—more than 10% of the mean—but they become much smaller when there is an internal pressure. To quantify the deviation d_{mean}, and understand how it arises from the particular curve shapes, we now study the $p = 0$ case in more detail.

4. Wrinkle Shape at Zero Pressure

Horizontal cross-sections of a deflated water balloon measured at equal vertical intervals above the seam are shown in Fig. 4A. Noting that the apparent profile of the top half of the balloon looks to be conical, we extrapolate an apex of the apparent profile from the side-view image. We then rescale the cross-sections by the distance to this apex. This simple rescaling nearly collapses
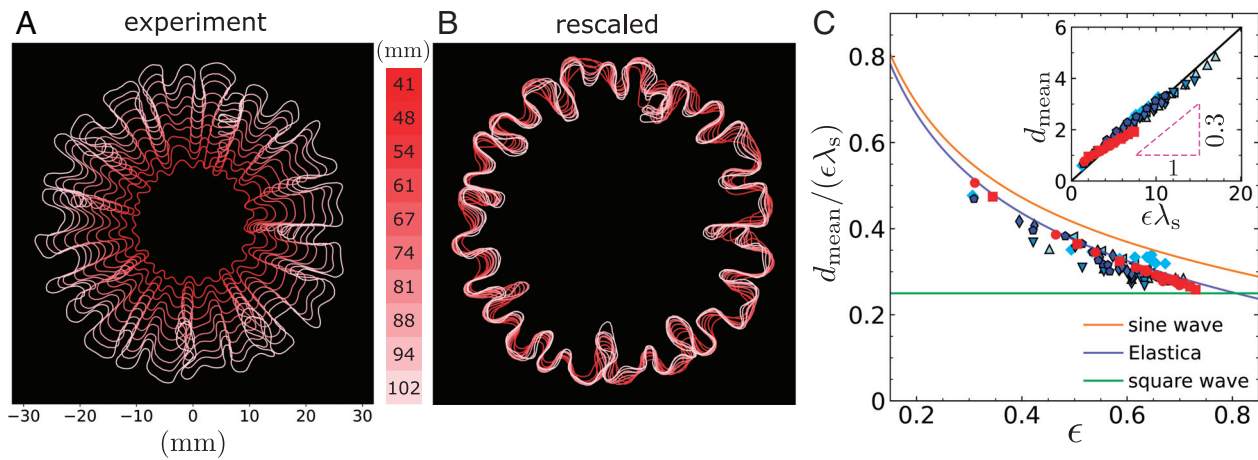
Fig. 4. Horizontal cross-sections in a deflated balloon exhibit a generalized conical structure. (*A*) Cross-section curves extracted from an balloon with $V_{water} = 112.9$ mL at $p = 0$, at 10 different heights. The contour is traced and plotted as a line for clarity. (*B*) Cross-sections rescaled by the distance to the extrapolated apex of the conical profile (this distance is denoted in the colorbar). This operation nearly collapses the rescaled shapes, indicating a generalized cone structure of the balloon structure. (*C*) Inset: the average protrusion, d_{mean}, of the cross-sections versus $\epsilon \lambda_s$ from experiments (blue) and the cross-section model (red). Units are mm; legend in Fig. 3C. The trend is approximately linear. Main: to examine these data in more detail, we plot $d_{mean}/(\epsilon \lambda_s)$ versus the effective strain ϵ, for various balloons at $p = 0$ from both the experimental measurements and the numerical predictions of the cross-section model. For comparison, we plot the exact relations for a sine wave, square wave, and Euler's Elastica, where in each case the amplitude is controlled by ϵ. The Elastica shows the best agreement with the data.

all the cross-sections (Fig. 4*B*), indicating that not only the gross shape but also the fine structure has the shape of a generalized cone.

A consequence of a conical structure is that the wrinkle wavenumber does not vary significantly with height z. To understand this observation, we assume that the selection of the wavelength is dominated by the tensional substrate stiffness (2), so that the wavelength scales as $\lambda \sim (B/T_s)^{1/4} r_{disk}^{1/2}$. If the wavenumber was to change with the height, the associated length scale ℓ would scale as $\ell \sim \lambda^2 \sqrt{T_s/B}$ (37). Taken together, $\ell \sim r_{disk}$, which explains the invariance of the wavenumber within the size of the balloon.

To study the shape of the individual cross-sections, we investigate the relations among the observables of the mean maximum amplitude d_{mean}, the wrinkle wavelength, and how much the cross-section is compressed. We define the material wavelength $\lambda_s \equiv 2\pi l_s/q$, which divides the total arclength of the cross-section by the number of undulations q, which we measure by counting peaks. We quantify the amount of compression by the effective strain $\epsilon \equiv (l_s - r_{mean})/l_s$ (to be contrasted with the local material strain, which is vanishingly small for our buckled films). Note that λ_s approaches the "usual wavelength", λ, when ϵ approaches 0. The particular shape of the undulations tells how d_{mean}, λ_s, and ϵ are related. For example, small-amplitude sinusoidal waves obey $d_{mean} \propto \sqrt{\epsilon} \lambda_s$ and for square waves $d_{mean} = \epsilon \lambda_s/4$. To examine the relation in our system, we plot d_{mean} versus $\epsilon \lambda_s$ in the inset to Fig. 4*C*. Remarkably, the data collapse onto a line that is fit well by:

$$d_{mean} \approx \beta \epsilon \lambda_s, \qquad [2]$$

where β is the linear coefficient with a best-fit value of 0.30.

The simple relation of Eq. **2** shows how to readily estimate the amplitude of wrinkles d_{mean} as a function of z. Given a volume of water, a washer radius, and a bag size, one may compute the arclength $l_s(z)$ and the mean shape $r_{mean}(z) \approx r_{gm}(z)$ with the geometric model. The crucial ingredient from the experiment is the observed wavenumber q (which is approximately independent of z). With just these parameters, one may then obtain $\epsilon(z)$ and

$\lambda_s(z)$, which combine via Eq. **2** to give $d_{mean}(z)$. This wrinkled envelope can be added to the mean shape to yield a predicted apparent shape. We do this in Fig. 2*E*; the result matches the experimental profile very well, especially when compared to the geometric model without the wrinkled envelope for the same balloon, in Fig. 2*D*. The correction continues to be favorable past the seam through the bottom of the balloon, which offers an explanation for the kink in the apparent profile at the location of the seam where the two disks are heat-sealed together. One might expect this kink is due to the larger rigidity of the heat-sealed seam. Instead, it arises from the triangular peak in the amount of material to be packed into the confined mean shape, since the excess length as a function of z grows linearly up to the location seam, and then falls linearly past the seam. Thus, it is a geometric and not a mechanical effect.

To examine the curves in more detail, we plot the ratio $d_{mean}/\epsilon \lambda_s$ as a function of ϵ in Fig. 4*C*. For comparison, we show the curves for sinusoidal waves, square waves, and the inflexional Elastica (38). The data are close to the trend for the Elastica—local minimizers of the integrated squared curvature, which capture the bending mechanics of an inextensible rod in equilibrium. This behavior is expected for confined isometric surfaces (39); in our case, the presence of tension along the wrinkles may introduce deviation to pure Elastica, as we will see.

Our detailed analyses of the cross-sections have two main conclusions: First, in contrast to hierarchical wrinkling such as in a suspended curtain (37, 40), here the cross-section shape is approximately independent of z (Fig. 4*B*). Second, the shared properties of the cross-sections with Elastica points to the relevance of a minimization of the bending energy within a cross-section. These findings motivate a quasi-two-dimensional model for a typical cross-section, which is representative of all the others in a given configuration of the balloon.

5. Quasi-Two-Dimensional Model

We model a cross-section of the balloon at l_s as an inextensible filament of total length $L = 2\pi l_s$. For a filament with a two-

dimensional, arc-length parametrized configuration $r(s)$, the bending energy is

$$U_b = \frac{B}{2} \int r''(s)^2 ds, \qquad \text{[3]}$$

where B is the bending rigidity.

Inspired by the "elastic foundation" effect induced by a longitudinal tension (2), we introduce a confinement energy

$$U_t = \frac{\eta T_s}{2r_{disk}^2} \int [r(s) - r_{id}(s)]^2 ds, \qquad \text{[4]}$$

penalizing deviations of the filament from an ideal configuration $r_{id}(s) = r_{conf} \cdot (\cos(s/L), \sin(s/L))$. Here, r_{conf} is a parameter to be determined by the solution of the geometric model. Crucially, we further incorporate the finite slope effect by penalizing both the radial and azimuthal deviations in the integrand of Eq. 4, without which the system configuration $r(s)$ would have favored a single deep fold (27, 41). To account for the doubly curved profile and the boundary connecting to the balloon membrane below the water level, we introduce a dimensionless factor η. To retain the predictive power, we set η to be a fixed numerical parameter independent of p, to be determined a posteriori by matching the configuration wavenumber q produced by the model with the experimental observation.

So far the model is for $p = 0$, but pressure can be incorporated by considering the work that it does on the filament. This work is p multiplied by the enclosed area, which reads:

$$U_p = -\frac{p}{2} \int r(s) \times r'(s) ds. \qquad \text{[5]}$$

The total energy associated with the model cross-section is then

$$U_{tot}[r(s)] = U_b + U_p + U_t. \qquad \text{[6]}$$

In computing U_t, the parameter r_{conf} is specified by requiring the case of an inextensible balloon membrane with zero bending rigidity to recover the prediction of the geometric model. Accordingly, for the representative filament with bending rigidity $B = 0$, $r(s)$ should approach a circle of radius r_{gm} with arbitrarily small and dense oscillations. The total energy becomes $\lim_{B \to 0} U_{tot}(r) = (\eta T_s)/(2r_{disk}^2)(r - r_{conf})^2 L - \pi p r^2$ and should take its minimum at $r = r_{gm}$. Setting $\partial_r \lim_{B \to 0} U_{tot}|_{r_{gm}} = 0$ gives

$$r_{conf} = r_{gm}\left(1 - \frac{1}{\eta}\frac{pr_{disk}^2}{T_s l_s}\right). \qquad \text{[7]}$$

In this flexible membrane limit, the balloon assumes a radius of r_{conf} at $p = 0$, while for $p > 0$ the pressure term U_p displaces the balloon radius to r_{gm}.

We are interested in finding the configuration $r(s)$ that minimizes the total energy $\delta U_{tot}[r(s)] = 0$. To realize the energy minimization, we derive the corresponding force $f_{tot}(s) = -\delta U_{tot}/\delta r(s)$ and evolve the configuration using the dynamics of an over-damped system $\partial_t r(s) = f_{tot}(s)$ to equilibrium. An "inextensibility force" is added to preserve the filament length L (42), as is a self-repulsion force against self-crossing (SI Appendix).

Fig. 3B shows the predictions of the filament model at various pressures. Qualitatively, the numerical configurations capture the lobe formation at high pressure, the rounded wrinkle shape at

low pressure, and a wrinkle-fold transition with wavenumber proliferation at intermediate pressure. For each configuration, the mean radius r_{mean}, similarly defined as in the experimental measurements, is computed and plotted in Fig. 3C as the red markers. The numerical minimization reproduces quantitatively that the mean radius of the filament is close to the prediction of the geometric model. Similarly, the mean amplitude d_{mean} of the filament protrusions is extracted and a quick decay over increasing pressure is manifest as shown in Fig. 3D. For all pressures, the wavenumber produced by the filament model increases with an increasing numerical coefficient η in Eq. 4. Nonetheless, the threshold pressure for the wrinkle-fold transition is insensitive to our choice of η (SI Appendix). Selecting an appropriate value of η allows us to match the entire $q(p)$ curve obtained in experiments, shown in the inset of Fig. 3C.

For the special case of $p = 0$, we extract $d_{mean}/\epsilon\lambda_s$ and ϵ from the model filaments, which we may compare with the experimental data in Fig. 4C. Although the numerical results are broadly consistent with the experiments, there is a small but noticeable deviation from the Elastica curve. Such distinction is irresolvable experimentally due to system noise, yet shall be expected from the longitudinal tension along the conical shape.

6. Shape of Deep Folds

We have seen that the minimal physical ingredients to reproduce the cross-section morphology are the effects of pressure, the bending energy within a cross-section, and an effective pinning potential that captures the coupling of cross-sections to the prediction of the geometric model. To further check the validity of this two-dimensional model, we turn to study the shape of individual folds at large pressure. At the tip of each fold, the membrane curves around sharply, shown in the cross-section as a small loop (Fig. 5A). We observe that the size and shape of the folds can vary between different folds at different pressures. To see whether there is a commonality among the folds, we scale and superimpose the loops onto each other by adding the brightness values of the photos. Remarkably, a master shape appears, as shown in Fig. 5B. The emergence of a common shape upon the scaling of the images suggests the existence of a mathematical similarity solution of the loop profile.

We notice that at high pressure, the loops become small with large curvature so that the total energy Eq. 6 of our model filament is dominated by the bending term U_b and the pressure term U_p. Minimizing $U_b + U_p$ (neglecting the pinning potential U_t), we obtain a differential equation for the loop shape (SI Appendix, 43, 44). We solve this equation numerically and plot the result as a solid curve on Fig. 5B, which is in excellent agreement with the composite experimental image. While qualitatively similar to loops in clamped elastica (45, 46), this precise shape results from a balance between bending and pressure.

Having settled the shape of the loops, we now investigate their size. Intuitively, we expect a balance between the bending and pressure effects to determine their width, leading to

$$w_{loop} = \xi\left(\frac{B}{p}\right)^{1/3}. \qquad \text{[8]}$$

This scaling also arises for ridges in depressurized shells on mandrels (47), and this result is supported by the full analysis of the filament model (SI Appendix), which further gives the value of the prefactor, $\xi = 1.065$. We measure the width of many loops at two different cross-section heights and at multiple values of air pressure. The blue symbols in Fig. 5C show the results,
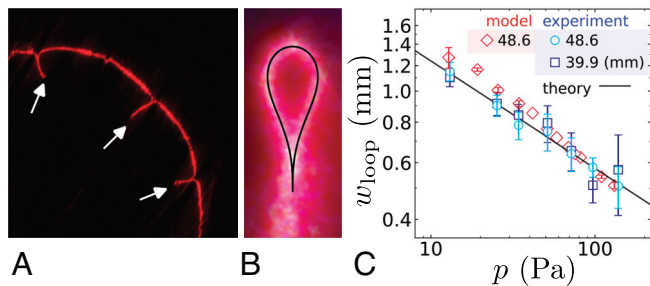
Fig. 5. Loops at the tips of folds at high pressure. (*A*) Self-contacting folds form in a pressurized balloon, imaged in a horizontal cross-section produced by laser scattering. Arrows indicate the location of folds. Each fold forms a small loop at its tip. (*B*) Superposition of 25 rescaled laser-scattering images of fold tips at various pressures, with $V_{\text{water}} = 103.5$ mL. Black curve: exact similarity solution in the high-pressure limit. (*C*) The loop width, w_{loop}, versus p. The data are an average of multiple loops at a given pressure; error bars show the variation in the observed loop size, quantified by the SD over the mean of the measurements. Experimental measurements at two different heights give consistent results. Results from the cross-section model (red markers) in the same conditions agree well with the experiments. Line: Exact model prediction in the high-pressure limit, using the value of $B = 1.58 \times 10^{-8}$ J that we measured (text).

where the error bars are computed as the SD of the mean. The data at two different z-positions, represented by two different shades of blue, fall on top of one another, once again supporting the local treatment of the cross-section model. All the data are in good agreement with the predicted scaling of Eq. **8** with pressure.

As a more stringent test, we may compare Eq. **8** directly with the data, by using a value of $B = (1.58 \pm 0.06) \times 10^{-8}$ J for the balloon material, which we obtained by measuring the Young's modulus E using a tensile tester, and using $B = Et^3/[12(1-\nu^2)]$ with $\nu = 0.4$ (*SI Appendix*). The prediction is in good agreement with the data (solid line in Fig. 5*C*). Conversely, one can use a power-law fit to the data to measure the bending modulus of the film. For our data, this yields a value of $B = (1.44 \pm 0.15) \times 10^{-8}$ J, which is a surprisingly accurate measurement.

Finally, we compare our results with the cross-section model, which incorporates the confinement term U_t in Eq. **6**. We generate cross-sections at multiple pressures and measure the width of the loops. The result, shown by the red markers in Fig. 5*C*, agrees well with the experiments.

7. Discussion

We have probed the gross shape, the fine structure, and the interplay between them in a balloon made of two flat elastic disks sealed at the edge, partly filled with water and pressurized. We have considered the geometric model that treats the sheet as inextensible yet free to compress, due to a vanishing bending modulus that allows for the formation of buckled fine structures at negligible energetic cost. We found that this model predicts the "mean shape" of the sheet, defined as the mean radius of the cross-sections. We have then shown that the undulations of the cross-sections around the mean shape are well-described by a phenomenological model that accounts for the resistance to bending, the effect of pressure, and a pinning to the mean shape. In particular, this model captures the transition between wrinkles resembling the Elastica at zero pressure to folds with a rounded tip when pressure is applied.

A wrinkle-fold transition is usually associated with the global compression exceeding a finite threshold value (28, 41). This threshold is predicted to be of the same scale of the wrinkle

wavelength (25), so that wrinkles typically become unstable to forming a fold at small slopes. Here, at zero pressure, we observe wrinkles that are stable up to large slopes, and at a global compression that is much larger than the wavelength. Notably, in our system, the transition to folding occurs as the azimuthal compression decreases, signaling a different mechanism than the well-studied wrinkle-fold transition that is driven by a growing wrinkle amplitude. Indeed, the transition to folds that we observe is due to the internal pressure that deforms the wrinkles, leading to self-contact. The ability of wrinkles to survive at large amplitude is rooted in the restoring force when the cross-section deviates from its ideal position, which has components both in the radial and angular directions.

There is another known class of wrinkle-fold transitions with a distinct geometric mechanism. In some settings, the energetically favored gross shape may break axisymmetry in such a way where some of the excess length must be stored locally. This scenario may be compatible with the formation of localized deep folds but not with regular wrinkles (17, 48). Our results show that a pressurized water balloon does not fall into this class: both wrinkles and folds serve to waste excess material length along an axisymmetric gross shape. Hence, our system displays an intriguing type of wrinkle-fold transition where wrinkles are stabilized by an isotropic tension term but destabilized by the internal pressure.

More generally, our results raise fundamental questions about the nature of convergence toward the shape predicted by the geometric model. The geometric model predicts the limiting shape of the sheet as the bending modulus B vanishes. This limiting shape has a compressive strain, which corresponds to infinitesimal undulations of the actual sheet around its mean shape (49). Previous works, which have focused on nearly planar shapes with small effective compressive strain have suggested that these undulations usually take the form of sinusoidal wrinkles (3, 34). Our observations show that, when the effective compressive strain is large, the undulations could also take the form of deep folds. Beyond the shape of the undulations, the convergence toward the prediction of the geometric model can be quantified by the evolution of the wavelength λ as $B \to 0$. For the tensional wrinkles that we observe, the wavelength should scale as $\lambda \sim B^{1/4}$ (2). For the tensional folds, a scaling argument leads to $\lambda_{\text{fold}} \sim B^{2/9}$ (*SI Appendix*) for the distance between folds. Since the loops at the tips of the folds follow $w_{\text{loop}} \sim B^{1/3}$, then $\lambda_{\text{fold}} \gg w_{\text{loop}}$ as the bending modulus vanishes, ensuring that the folds remain spatially separated in this limit.

Materials and Methods

To construct the balloons, disks of radius 83 mm are cut from polyethylene produce bags of thickness $t = 8.0 \pm 0.8$ µm or from plastic food wraps with $t = 10.2 \pm 0.8$ µm. The stress-strain curves for the sheets are measured with a tensile tester (Test Resources, 250 lbs actuator). Depending on the direction of measurement, we obtain Young's moduli for the sheets to vary between $E = 315$ MPa and 1,103 MPa for produce bags and between $E = 89$ MPa and 195 MPa for food wraps. The measurements are detailed in *SI Appendix*. An air-tight seal is formed by pressing a heated iron ring of diameter 166 mm onto the double layer. The balloon is then filled with water and air and suspended from the top center. Despite the anisotropy of the Young's modulus measured in the balloon membrane, we do not see large systematic variations in the morphological behaviors in a suspended balloon as a function of angle of loading. Side views of the balloons are photographed with a Nikon DLSR with backlighting from an LED white screen.

To obtain the horizontal cross-sections, we illuminate a slice of the balloon with a horizontal sheet of laser light, and we photograph the scattered light

from the side at an oblique angle. A calibrated perspective transformation is then applied to produce the final horizontal image. To better capture the back of the balloon, we reflect a portion of the light sheet onto the back of the system with two vertical mirrors. The above procedure is sometimes repeated from different azimuthal angles and the results are superimposed, to reduce noise and better capture the back of the balloon. The images captured from different angles collapse well on one another, indicating that the cross-sections are obtained accurately without geometric distortion.

1. E. Cerda, K. Ravi-Chandar, L. Mahadevan, Thin films: Wrinkling of an elastic sheet under tension. *Nature* **419**, 579–580 (2002).
2. E. Cerda, L. Mahadevan, Geometry and physics of wrinkling. *Phys. Rev. Lett.* **90**, 074302 (2003).
3. B. Davidovitch, R. D. Schroll, D. Vella, M. Adda-Bedia, E. A. Cerda, Prototypical model for tensional wrinkling in thin sheets. *Proc. Natl. Acad. Sci. U.S.A.* **108**, 18227–18232 (2011).
4. K. Matan, R. B. Williams, T. A. Witten, S. R. Nagel, Crumpling a thin sheet. *Phys. Rev. Lett.* **88**, 076101 (2002).
5. D. L. Blair, A. Kudrolli, Geometry of crumpled paper. *Phys. Rev. Lett.* **94**, 166107 (2005).
6. G. A. Vliegenthart, G. Gompper, Forced crumpling of self-avoiding elastic sheets. *Nat. Mater.* **5**, 216–221 (2006).
7. T. A. Witten, Stress focusing in elastic sheets. *Rev. Mod. Phys.* **79**, 643–675 (2007).
8. J. Hure, B. Roman, J. Bico, Stamping and wrinkling of elastic plates. *Phys. Rev. Lett.* **109**, 054302 (2012).
9. B. Roman, A. Pocheau, Stress defocusing in anisotropic compaction of thin sheets. *Phys. Rev. Lett.* **108**, 074301 (2012).
10. I. Tobasco et al., Exact solutions for the wrinkle patterns of confined elastic shells. *Nat. Phys.* **18**, 1099–1104 (2022).
11. J. Chopin, A. Kudrolli, Helicoids, wrinkles, and loops in twisted ribbons. *Phys. Rev. Lett.* **111**, 174302 (2013).
12. J. Chopin, V. Démery, B. Davidovitch, Roadmap to the morphological instabilities of a stretched twisted ribbon. *J. Elast.* **119**, 137–189 (2015).
13. A. Legrain, E. J. Berenschot, L. Abelmann, J. Bico, N. R. Tas, Let's twist again: Elasto-capillary assembly of parallel ribbons. *Soft Matter* **12**, 7186–7194 (2016).
14. D. P. Holmes, A. J. Crosby, Draping films: A wrinkle to fold transition. *Phys. Rev. Lett.* **105**, 038303 (2010).
15. S. Knoche et al., Elastometry of deflated capsules: Elastic moduli from shape and wrinkle analysis. *Langmuir* **29**, 12463–12471 (2013).
16. D. Vella, J. Huang, N. Menon, T. P. Russell, B. Davidovitch, Indentation of ultrathin elastic films and the emergence of asymptotic isometry. *Phys. Rev. Lett.* **114**, 014301 (2015).
17. J. D. Paulsen et al., Optimal wrapping of liquid droplets with ultrathin sheets. *Nat. Mater.* **14**, 1206–1209 (2015).
18. J. D. Paulsen, Wrapping liquids, solids, and gases in thin sheets. *Ann. Rev. Condens. Matter Phys.* **10**, 431–450 (2019).
19. E. Siéfert, E. Reyssat, J. Bico, B. Roman, Programming curvilinear paths of flat inflatables. *Proc. Natl. Acad. Sci. U.S.A.* **116**, 16692–16696 (2019).
20. M. M. Ripp, V. Démery, T. Zhang, J. D. Paulsen, Geometry underlies the mechanical stiffening and softening of an indented floating film. *Soft Matter* **16**, 4121–4130 (2020).
21. Y. Timounay et al., Sculpting liquids with ultrathin shells. *Phys. Rev. Lett.* **127**, 108002 (2021).
22. E. H. Mansfield, *The Bending and Stretching of Plates* (1989).
23. V. A. Gorkavyy, On inflating closed mylar shells. *Comptes Rendus Mécanique* **338**, 656–662 (2010).
24. J. D. Paulsen et al., Curvature-induced stiffness and the spatial variation of wavelength in wrinkled sheets. *Proc. Natl. Acad. Sci. U.S.A.* **113**, 1144–1149 (2016).
25. H. Diamant, T. A. Witten, Compression induced folding of a sheet: An integrable system. *Phys. Rev. Lett.* **107**, 164302 (2011).
26. F. Brau et al., Multiple-length-scale elastic instability mimics parametric resonance of nonlinear oscillators. *Nat. Phys.* **7**, 56–60 (2011).
27. V. Démery, B. Davidovitch, C. D. Santangelo, Mechanics of large folds in thin interfacial films. *Phys. Rev. E* **90**, 042401 (2014).
28. O. Oshri, F. Brau, H. Diamant, Wrinkles and folds in a fluid-supported sheet of finite size. *Phys. Rev. E* **91**, 052408 (2015).
29. I. Pak, J. M. Schlenker, Profiles of inflated surfaces. *J. Nonlinear Math. Phys.* **17**, 145–157 (2010).
30. G. I. Taylor, "On the shapes of parachutes (paper written for the Advisory Committee for Aeronautics, 1919)" in *The Scientific Papers of Sir Geoffrey Ingram Taylor*, G. K. Batchelor, Ed. (Cambridge University Press, New York, 1963), vol. 3, pp. 26–37.
31. J. H. Smalley, "Determination of the shape of a free balloon. balloons with superpressure, subpressure and circumferential stress: and capped balloons" (Tech. rep., Litton Systems Inc St Paul MN, 1964).
32. F. Baginski, T. Williams, W. Collier, A parallel shooting method for determining the natural shape of a large scientific balloon. *SIAM J. Appl. Math.* **58**, 961–974 (1998).
33. F. Baginski, Nonuniqueness of strained ascent shapes of high altitude balloons. *Adv. Space Res.* **33**, 1705–1710 (2004).
34. H. King, R. D. Schroll, B. Davidovitch, N. Menon, Elastic sheet on a liquid drop reveals wrinkling and crumpling as distinct symmetry-breaking instabilities. *Proc. Natl. Acad. Sci. U.S.A.* **109**, 9716–9720 (2012).
35. J. R. Dormand, P. J. Prince, A family of embedded Runge-Kutta formulae. *J. Comput. Appl. Math.* **6**, 19–26 (1980).
36. P. Virtanen et al., SciPy 1.0: Fundamental algorithms for scientific computing in Python. *Nat. Methods* **17**, 261–272 (2020).
37. H. Vandeparre et al., Wrinkling hierarchy in constrained thin sheets from suspended graphene to curtains. *Phys. Rev. Lett.* **106**, 224301 (2011).
38. A. E. H. Love, *A Treatise on the Mathematical Theory of Elasticity* (Cambridge University Press, ed. 2, 1906), pp. 384–388.
39. E. Cerda, L. Mahadevan, Confined developable elastic surfaces: Cylinders, cones and the Elastica. *Proc. R. Soc. A: Math. Phys. Eng. Sci.* **461**, 671–700 (2005).
40. R. D. Schroll, E. Katifori, B. Davidovitch, Elastic building blocks for confined sheets. *Phys. Rev. Lett.* **106**, 074301 (2011).
41. L. Pocivavsek et al., Stress and fold localization in thin elastic membranes. *Science* **320**, 912–916 (2008).
42. A. K. Tornberg, M. J. Shelley, Simulating the dynamics and interactions of flexible fibers in stokes flows. *J. Comput. Phys.* **196**, 8–40 (2004).
43. L. D. Landau, E. Lifshitz, *Theory of Elasticity, Course of Theoretical Physics* (Elsevier, New York, ed. 3, 1986), vol. 7, p. 109.
44. J. E. Flaherty, J. B. Keller, S. I. Rubinow, Post buckling behavior of elastic tubes and rings with opposite sides in contact. *SIAM J. Appl. Math.* **23**, 446–455 (1972).
45. C. Py et al., Capillary origami: Spontaneous wrapping of a droplet with an elastic sheet. *Phys. Rev. Lett.* **98**, 156103 (2007).
46. A. E. Cohen, L. Mahadevan, Kinks, rings, and rackets in filamentous structures. *Proc. Natl. Acad. Sci. U.S.A.* **100**, 12141–12146 (2003).
47. J. Marthelot, P. T. Brun, F. L. Jiménez, P. M. Reis, Reversible patterning of spherical shells through constrained buckling. *Phys. Rev. Mater.* **1**, 025601 (2017).
48. J. D. Paulsen et al., Geometry-driven folding of a floating annular sheet. *Phys. Rev. Lett.* **118**, 048004 (2017).
49. I. Tobasco, Curvature-driven wrinkling of thin elastic shells. *Arch. Ration. Mech. Anal.* **239**, 1211–1325 (2021).